

TeraFET terahertz detectors with spatially non-uniform gate capacitances

Yuhui Zhang and Michael S. Shur ^{a)}

*Department of Electrical, Computer and Systems Engineering, Rensselaer Polytechnic Institute,
Troy, New York 12180 USA*

^{a)} Author to whom correspondences should be addressed. E-mail: shurm@rpi.edu

ABSTRACT

A non-uniform capacitance profile in the channel of a THz field-effect transistor (TeraFET) could significantly improve the THz detection performance. The analytical solutions and simulations of the hydrodynamic equations for the exponentially varying capacitance versus distance showed ~10% increase in the responsivity for the 130 nm Si TeraFETs in good agreement with numerical simulations. Using the numerical solutions of the hydrodynamic equations, we compared three different C_g configurations (exponential, linear and sawtooth). The simulations showed that the sawtooth configuration provides the largest response tunability. We also compared the effects of the non-uniform capacitance profiles for Si, III-V, and p-diamond TeraFETs. The results confirmed a great potential of p-diamond for THz applications. Varying the threshold voltage across the channel could have an effect similar to that of varying the gate-to-channel capacitance. The physics behind the demonstrated improvement in THz detection performance is related to breaking the channel symmetry by device geometry of composition asymmetry.

The generation and detection of terahertz (THz) radiation has been a very active area over the recent decades¹⁻⁴. Occupying the frequency range of 100 GHz-30 THz, THz radiation fills the frequency gap between the electronics and photonics. Initially, THz science and technology were explored in the field of astronomy^{1,5}, and expanded rapidly since 1990s following the development of THz spectroscopy^{6,7}. By now, the real-life applications of THz-based technology can be found in various fields, including the biomedical engineering^{6,8}, VLSI testing⁹, wireless communication¹⁰⁻¹², and object sensing^{13,14}.

A high-quality THz signal detector plays a crucial role in almost all THz applications. The present-day THz sensors are mostly semiconductor-based, with Schottky devices being the dominant product^{1,15}. Recently, plasma-wave field-effect transistor (FET) detectors have attracted more attention as they offer high responsivity, ultra-fast response time, and are highly tunable by gate, doping, and channel structures¹⁶⁻¹⁹. Moreover, plasma-wave THz FETs (TeraFETs) are particularly promising for next-generation communication

applications, since these devices exhibited exceptional detection performance in the 200-400 GHz band allocated for beyond-5G communication^{10,11,20}.

Despite all those merits, plasmonic TeraFETs still face a variety of challenges, including the fabrication burden, requirement for high sensitivity, and noise issues^{18,21}. Among others, the detection sensitivity/responsivity is always a key issue. Due to the existence of scattering, the response voltage of TeraFETs can be limited, which impairs the device performance²²⁻²⁴. As was discussed in [25], further improvement in the TeraFET responsivity is required to enable their application in 6G communication. In this paper, we show that the implementation of a spatially non-uniform gate capacitance (C_g) profile could significantly enhance the responsivity. A non-uniform C_g profile can be realized by altering the barrier layer width. For example, consider a Si FET with a composite barrier layer of SiO₂ and HfO₂²⁶⁻²⁸. We may profile the HfO₂ layer by adjusting the etch rate²⁹ to achieve a non-uniform $C_g(x)$ (see Section A of Supplementary Material).

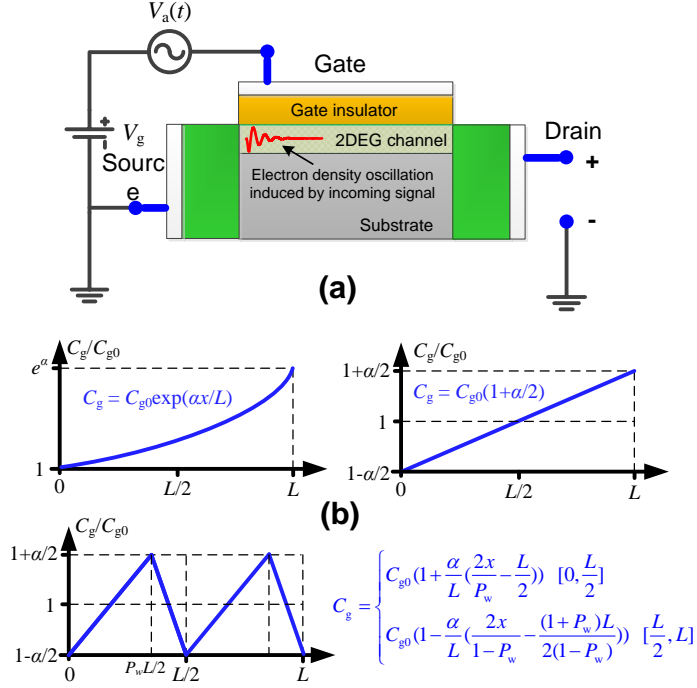


Fig. 1. (a) Schematic of THz detection by a TeraFET. $V_a(t)$ represents the radiation-induced AC small signal, and V_g is the DC gate voltage. (b) illustrations of 3 coordinate-dependent gate capacitance (C_g) configurations. C_{g0} is the initial constant gate capacitance, α is a modulation factor indicating the total variation of C_g along the channel, P_w is the ratio of rising edge period in one section, L is the channel length. The sawtooth C_g configuration in (b) contains two segments ($N_s=2$). In the simulations of this work, N_s is variable.

Under the DC operation, the gate voltage (V_g) and C_g determine the 2D carrier concentration (n). Following the unified charge control model (UCCM), the relation between n and V_g can be approximated as³⁰⁻³²:

$$n(U) = \frac{C_g \eta V_t}{e} \ln\left(1 + \exp\left(\frac{U}{\eta V_t}\right)\right) \quad (1)$$

where $V_t = k_B T / e$ is the thermal voltage (k_B : Boltzmann constant, T : temperature, fixed at 300 K). η is a subthreshold ideality factor. $U = V_g - V_{th} - \varphi$ is the gate-to-channel potential. V_{th} is the threshold voltage, and φ is the channel potential. Well above threshold ($U \gg V_t$), UCCM reduces to $n = CU/e$. Given a spatially non-uniform C_g , the steady-state density n_0 also becomes coordinate-dependent, creating a carrier gradient along the channel at zero drain bias. The existence of density gradient changes the transport of carriers, thus affecting the detection performance of TeraFETs. When we only alter C_g , V_{th} also changes. A non-uniform V_{th} can also modify the device characteristics, speed³³, and THz detection performance^{34,35}. For now we

assume that V_{th} is fixed under a varying C_g . The constant V_{th} can be achieved by adjusting the doping level in the device channel^{36,37}.

The boundary conditions beneficial for a plasma instability are the fixed source voltage of the TeraFET and the drain is fed a current source³⁸⁻⁴⁰. The Dyakonov-Shur instability occurs due to the difference in the reflection coefficients of the plasma wave from the drain and source sides of the channel. The resulting amplification factor is $(S_e + V_0)/(S_e - V_0)$, where S_e is the plasma wave velocity and V_0 is the DC drift velocity. This leads to the generation of plasma instability and the THz radiation^{38,41,42}. A non-uniform C_g profile affects the plasma velocity as well as the local Mach number ($M = V_0/S_e$), leading to changes in the amplification factor and the instability growth rate^{35,40}. We can therefore adjust the $C_g(x)$ profile to elevate the emitted THz power from TeraFETs and expand the dynamic range of instability regime.

Under the THz detection regime illustrated by Fig. 1(a), the source of the TeraFET is grounded while the drain is open. The plasma wave is initiated

at the source and travels towards the drain. The wave gets reflected at the drain without amplification if no DC current source is connected⁴³. Due to the nonlinearity of the resonant (or overdamped plasma oscillations) and the boundary conditions breaking symmetry, the AC response is rectified, inducing a DC voltage at the drain which is proportional to the intensity of the impinging THz radiation (at relatively low intensities). Both the DC response voltage and the plasma instability originate from the carrier density oscillations, and their amplitudes are limited by the nonlinearity of the hydrodynamic system⁴⁴. For the plasma instability operation, the transport and amplitude of plasma wave are affected by the non-uniform C_g structure^{40,45}. Therefore, we expect that a non-uniform C_g could also alter the continuous-wave THz detection performance of TeraFETs.

To evaluate in more details the effects of varying C_g on the detection performance, we solve the hydrodynamic equations^{30,46}:

$$\frac{\partial n}{\partial t} + \nabla \cdot (n\mathbf{v}) = 0 \quad (2)$$

$$\frac{\partial \mathbf{v}}{\partial t} + (\mathbf{v} \cdot \nabla)\mathbf{v} + \frac{e}{m}\nabla U + \gamma\mathbf{v} = 0 \quad (3)$$

Here, \mathbf{v} and m represent the hydrodynamic velocity and effective mass of the carrier, respectively. $\gamma = 1/\tau$ is the momentum relaxation rate, $\tau = 1/\gamma = \mu m/e$ is the momentum relaxation time, and μ is the field-effect mobility. The energy transport equation is ignored as we fix the operation temperature at 300 K and assume thermal equilibrium. The boundary conditions presented in Fig. 1(a), are $U(0,t) = U_0 + V_a$ and $J(L,t) = 0$, where $U_0 = V_g - V_{th}$ is the DC gate-to-source voltage above threshold, L is the channel length. $V_a = V_{am}\sin(\omega t)$ is an AC small signal voltage generated by the THz radiation shining onto the device.

In the sub-THz range and at room temperature, the TeraFETs typically operate in the non-resonant regime ($\omega\tau \ll 1$). Under this circumstance, $\partial V/\partial t \ll \gamma v$, and thus Eq. (3) reduces to^{47,48}

$$\mathbf{v} = -\frac{e\tau}{m}\nabla U = -\mu\nabla U \quad (4)$$

Solving (4) together with (1) and (2) assuming a 1-D geometry, and recognizing that $C_g(x)$ is spatially non-uniform, we get:

$$\frac{\partial n}{\partial t} - S_e^2 \tau \left(\frac{\partial^2 n}{\partial x^2} - \frac{\partial(\alpha_1 n)}{\partial x} \right) = 0 \quad (5)$$

where $\alpha_1 = (1/C_g)(\partial C_g/\partial t)$ is a gate capacitance modulation factor, S_e is the plasma wave velocity given by $S_e = \sqrt{\frac{\eta e V_t}{m} (1 + \exp(-\frac{U}{\eta V_t})) \ln(1 + \exp(\frac{U}{\eta V_t}))}$. For the small signal operation, one can assume $S_e(U) = S_e(U_0)$.

Inspecting Eq. (5), we can see that the non-uniform C_g affects the carrier distribution via α_1 and the term $\partial(\alpha_1 n)/\partial x$. For uniform C_g , $\partial(\alpha_1 n)/\partial x = 0$ and Eq. (5) reduces to Eq. (10) in [47]. Note that both α_1 and $\partial\alpha_1/\partial x$ are functions of x , given an arbitrary $C_g(x)$ profile, the solution of n can be highly nonlinear. To reduce the analytical burden, we first consider a constant α_1 (i.e. $C_g(x)$ is an exponential function of x). With this simplification, Eq. (5) can be solved together with the boundary conditions. We convert the voltage boundary conditions into their density counterparts, and expand with respect to V_{am} ⁴⁷:

$$\left\{ \begin{array}{l} n(0,t) \approx \begin{cases} \frac{C_g \eta V_t}{e} \exp(\frac{U_0}{\eta V_t}) (1 + \frac{V_{am} \cos \omega t}{\eta V_t} + \frac{V_{am}^2}{4(\eta V_t)^2}) & (\text{sub-}V_m) \\ \frac{C_g (U_0 + V_{am} \cos \omega t)}{e} & (\text{above } V_m) \end{cases} \\ \left. \left(\frac{\partial n}{\partial x} - \alpha_1 n \right) \right|_{x=L} = 0 \end{array} \right. \quad (6)$$

Solving Eq. (5) together with (6) under the subthreshold condition, averaging the solution of n over time, and comparing with previous response solutions²⁴, we obtain a semi-empirical solution for DC response voltage (dU , the DC source-to-drain voltage) (see Section B of Supplementary Material for detailed derivations):

$$dU = \frac{eV_{am}^2}{4mS_e^2} \left(1 + \beta - \frac{1 + \beta \cos(2k_1 L)}{\cosh(k_1 L) \cosh(k_2 L)} \right) \quad (7)$$

where

$$\left\{ \begin{array}{l} k_1 = \frac{\alpha_1}{2} + \sqrt{\left(\frac{\alpha_1}{2}\right)^2 + ik_0^2} \\ k_2 = \frac{\alpha_1}{2} + \sqrt{\left(\frac{\alpha_1}{2}\right)^2 - ik_0^2} \end{array} \right. \quad (8)$$

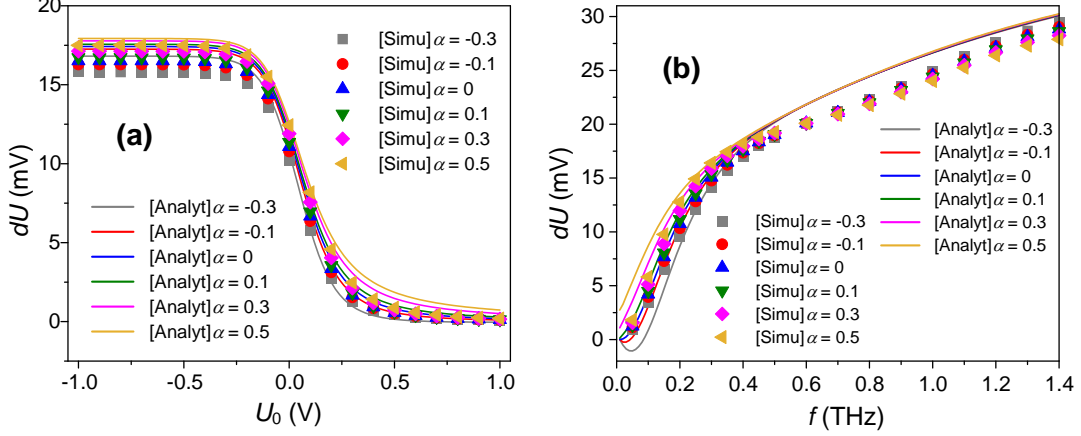


Fig. 2. (a) DC response voltage (dU) as a function of DC gate bias ($U_0 = V_{g0} - V_{th}$) under the radiation frequency $f = 350$ GHz and (b) dU as a function of f under $U_0 = -0.4$ V. Si TeraFETs, parameters: $m/m_0 = 0.19$, $\mu = 0.1$ m²/Vs, $L = 130$ nm. $C_g = C_{g0}\exp(\alpha x/L)$, with $\alpha = -0.3\sim 0.5$. The solid lines represent analytical curves, while scatters are simulation data points.

are complex wave numbers, $\beta = 1/\sqrt{1+(\omega\tau)^2}$.

$$k_r = \frac{\alpha_1}{2} + \sqrt{\frac{(\frac{\alpha_1}{2})^4 + k_0^4 + (\frac{\alpha_1}{2})^2}{2}}$$

is the real part of k_1 or

k_2 . $k_0 = \sqrt{\omega/S_c^2\tau}$ is the amplitude of k in uniform C_g channels.

Eq. (7) has a similar form as the expression of dU under a uniform C_g (see Eq. (24) in [24]). The main difference lies in the dispersion relation and wave numbers. This indicates that a non-uniform C_g changes the transport and decay features of collective carrier waves in the TeraFETs. As α_1 increases, k_r also rises, suggesting that the channel can now accommodate more full waves (or a larger total phase of wave(s)). With more “ups and downs” in the channels, the DC component could develop more efficiently.

To validate the theory proposed above, we compare the theory results with numerical simulations. The model used for simulation is the same as the one in [22], except that we assume thermal equilibrium here and ignore the energy relaxation equation. This model has been validated with the experimental data and proved to be effective^{22,43,49}. Fig. 2(a) shows the simulated and analytical dU as a function of U_0 for Si TeraFETs under $f = 350$ GHz. The spatial distribution of C_g is designed as $C_g = C_{g0}\exp(\alpha x/L)$, where C_{g0} is a constant capacitance, α is the C_g modulation factor. Under this configuration, $\alpha_1 = \alpha/L$. As seen in Fig.

2(a), the simulated dU data show the same variation trend as that of analytical curves, i.e. the response increases with the decrease of U_0 , and saturates in the subthreshold region. It is worth noting that this U_0 dependence profile results from the infinite load resistance (ideal open drain) and zero gate leakage current. For a finite load resistance or a non-zero leakage current, the response will be attenuated in the deep subthreshold region due to the dramatic increase of the channel resistance (see Section C of Supplementary Material for more details). Moreover, both simulation and analytical results show that dU increases with rising α in the subthreshold region. Beyond threshold, the α -dependence of dU weakens as U_0 increases. However, the effect of a non-uniform profile is significant near the threshold, where most TeraFET THz detector operate.

Fig. 2(b) shows the frequency (f) dependence of dU under different α values at $U_0 = -0.4$ V. A good qualitative (even quantitative) agreement between the simulation and analytical results is observed at $f < 400$ GHz ($\omega\tau \ll 1$, deep non-resonant region). The best agreement is achieved within 200-400 GHz band, overlapping the frequency range of beyond-5G communication. For $f > 500$ GHz, the Si device approaches the resonant regime, and thus the analytical curves deviate from the simulation data. But the general variation trend remains the same. In the non-resonant region, a larger α leads to a larger

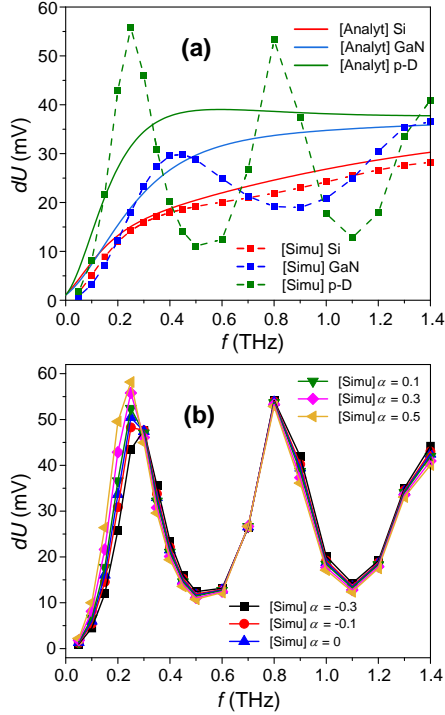


Fig. 3. dU as a function of f for (a) TeraFETs of Si and WBG materials (GaN and p-Diamond) under $\alpha = 0.3$ and (b) p-Diamond TeraFETs with $\alpha = -0.3 \sim 0.5$. $U_0 = -0.4$ V, $L = 130$ nm, $C_g = C_{g0} \exp(\alpha x/L)$.

dU . While for $f > 500$ GHz, the α dependence of dU gradually reverses with the increase of frequency, as presented in Fig. 2(b) by the simulation data. In the analytical theory, if we change the signs of square root terms in k_1 and k_2 (corresponding to another pair of solution of the dispersion equation), the α dependence of dU also reverses. Therefore, we may attribute the reversal of α dependence to the changes in wave propagation properties as the device enters the resonant mode. The results in Fig. 2 demonstrate that we successfully manipulated the DC response of a Si FET by an exponential C_g structure under subthreshold, non-resonant condition, and the proposed analytical theory shows a fair agreement with the simulation results.

Fig. 3(a) shows the frequency dependence of dU under different α values for Si, AlGaIn/GaN and p-Diamond (p-D) TeraFETs. The material parameters used are given in Table I. We can see that for p-D and AlGaIn/GaN devices, the resonant peaks are observed, and thus the simulation results exhibit more significant deviation from the analytical curves compared to Si FET. Indeed, with larger

effective masses and mobilities, the plasmonic resonance ($\omega\tau \geq 1$) can be achieved at much lower frequencies in wide-band-gap (WBG) materials compared to those in Si (see values of $\gamma/2\pi$ in Table I). Moreover, the p-D TeraFET exhibits the largest dU within the sub-THz region, reflecting its advantage in detection sensitivity over other materials. This observation conforms to our previous results in [20] and [21]. Fig. 3(b) illustrates the dU as a function of f for p-D TeraFETs under different α values. For $f < 300$ GHz, dU still increases with the rise of α . Beyond 300 GHz, a much weaker α dependence is observed. Note that the fundamental resonance is reached at around 250 GHz, thus the modulation of dU by C_g at the resonant regime is achieved. At $f = 250$ GHz, dU increases from 50.4 mV to 58.2 mV as α rises from 0 to 0.5, showing a 15% elevation. While for Si FETs, the increment is 12.9% (13.2 mV to 14.9 mV). Those data further demonstrated the potential advantages of p-D over other materials for plasmonic sub-THz detection applications.

Table I. Material parameters used in this work. (Note: d_b and ϵ_r are the thickness and permittivity of dielectric barrier layer, respectively. ν is the kinematic viscosity)

Material	Si MOS	AlGaIn/GaN	p-D
m/m_0	0.19	0.23	0.663
μ (m ² /Vs)	0.1	0.2	0.2
$\gamma/2\pi$ (THz)	1.47	0.61	0.21
d_b (nm)	4	20	4
ϵ_r	3.9	5.7	8.9
ν (cm ² /s)	5.6	4.6	1.6
Reference	[50-52]	[53-55]	[21,56,57]

To improve the tunability of dU by C_g , it is intuitive to explore other C_g profiles. Here we compare the detection performance of Si TeraFETs under 3 configurations (exponential, linear and sawtooth, see Fig. 1(b)). For non-exponential C_g profiles, α_1 is a function of x , and thus the term $n \cdot \partial\alpha_1/\partial x$ becomes non-zero and contributes to the transport. This provides additional possibility for the dU manipulation. Fig. 4(a) shows dU as a function of α under different configurations. As seen, the dU profile under linear configuration is

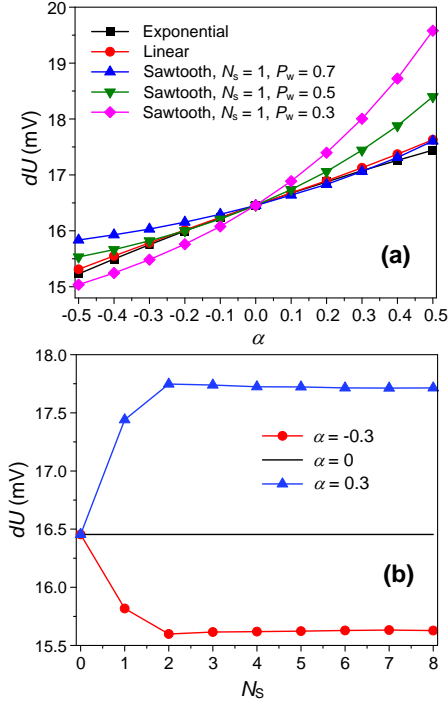


Fig. 4. Simulation results of dU for Si TeraFETs (a) as a function of α under different C_g configurations and (b) dU as a function of N_s with sawtooth profile under $P_w = 0.5$. P_w is the ratio of rising edge period in each segment. $f = 350$ GHz, $U_0 = -0.4$ V.

similar to that of exponential configuration. However, the tunability of sawtooth configuration appears to be significantly better than other two, as the response can be tuned by various parameters: α , P_w (the ratio of rising edge) and N_s (number of segments). With the decrease of P_w , the tunability of dU by α enhances. If N_s increases, the α -tunability also improves, as shown in Fig. 4(b), where the maximum tunability is observed at $N_s = 2$. Beyond $N_s = 2$, the simulated dU saturates. The above response characteristics under different $C_g(x)$ profiles is related to the changes in $\alpha_1(x)$ as the parameters alter. Fig. 5 illustrates the spatial distribution of $\alpha_1(x)$ for linear, exponential, and sawtooth $C_g(x)$ configurations. Apparently, α_1 curves of sawtooth profiles in Fig. 5(b) exhibit larger peak values and more violent oscillations compared to those of linear and exponential configurations shown in Fig. 5(a). This might be the reason why a sawtooth $C_g(x)$ has a better dU tunability than other configurations. As N_s and P_w changes, the peaks and ratios of positive and negative regions in $\alpha_1(x)$ could change significantly,

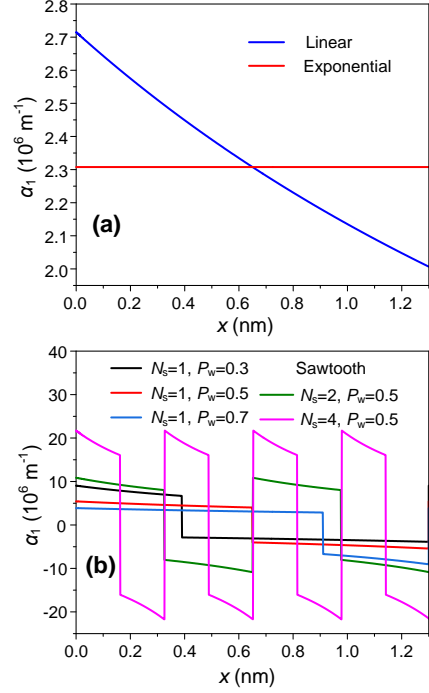


Fig. 5. The spatial distribution of α_1 for (a) linear and exponential $C_g(x)$ profiles and (b) sawtooth profiles. Parameters: $L = 130$ nm, $\alpha = 0.3$.

as shown in Fig. 5(b), which further modifies the detection performance.

In addition to the non-uniform C_g structures, the manipulation of DC response can also be achieved by a spatially non-uniform threshold voltage V_{th} under a uniform C_g . The non-uniform V_{th} can be achieved by the doping modulation^{36,37}. To analytically evaluate the effects of non-uniform V_{th} , we consider the original form of Navier-Stocks equation for carriers⁵⁸:

$$\frac{\partial \mathbf{v}}{\partial t} + (\mathbf{v} \cdot \nabla) \mathbf{v} + \gamma \mathbf{v} = \frac{e}{m} \nabla \varphi \quad (9)$$

Note that $U = V_g - V_{th} - \varphi$, for a uniform V_{th} , $\Delta \varphi = -\Delta U$ and (9) reduces to (3). With a non-uniform V_{th} , we obtain

$$\frac{\partial \mathbf{v}}{\partial t} + (\mathbf{v} \cdot \nabla) \mathbf{v} + \gamma \mathbf{v} + \frac{e}{m} (\nabla U + \nabla V_{th}) = 0 \quad (10)$$

and under the non-resonant operation (10) reduces to

$$\mathbf{v} = -\frac{e\tau}{m} (\nabla U + \nabla V_{th}) \quad (11)$$

Combining (11) and (2), we obtain (see Section D of Supplementary Material)

$$\frac{\partial n}{\partial t} - S_e^2 \tau \frac{\partial^2 n}{\partial x^2} - S_0^2 \tau \frac{\partial (\alpha_1^* n)}{\partial x} = 0 \quad (12)$$

Where we define $\alpha_1^* = \frac{1}{|V_{th0}|} \frac{\partial V_{th}}{\partial x}$, $S_0 = \sqrt{\frac{e|V_{th0}|}{m}}$.

Eq. (12) has a similar form as Eq. (5) and can be solved by the same method. Now the detection performance is controlled by α_1^* . (12) and (5) becomes identical when

$$S_e^2 \alpha_1 + S_0^2 \alpha_1^* = 0 \quad (13)$$

Eq. (13) indicates that α_1^* needs to be negative in order to improve the detection sensitivity. i.e. the threshold voltage should decrease from source to the drain so as to elevate dU .

In conclusion, we successfully manipulated the DC voltage response of TeraFETs by non-uniform capacitance profiles, and proposed a theory to qualitative explain this phenomena. The analytical calculations showed a good agreement with the simulation data under the non-resonant, subthreshold condition. In general, the DC response voltage is elevated if C_g rises from source to drain. We compared the modulation performances of 3 different $C_g(x)$ profiles and found that a sawtooth configuration exhibited the largest response tunability. The manipulation of DC response can also be achieved by a spatially non-uniform threshold voltage. Those discoveries could help improve the responsivity of plasmonic TeraFET detectors and promote their industrial applications.

SUPPLEMENTARY MATERIAL

See Supplementary Material for details of gate capacitance profiling, derivations of DC response voltage, and the effects of device loading and gate leakage current.

DATA AVAILABILITY

The data that support the findings of this study are available from the authors upon reasonable request.

REFERENCES

- ¹ S. S. Dhillon, M. S. Vitiello, E. H. Linfield et al., *Journal of Physics D: Applied Physics* **50** (4), 043001 (2017).
- ² R. A. Lewis, *Journal of Physics D: Applied Physics* **52** (43), 433001 (2019).
- ³ Wojciech Knap, Mikhail Dyakonov, Dominique Coquillat et al., *Journal of Infrared, Millimeter, and Terahertz Waves* **30**, 1319 (2009).
- ⁴ Michael S. Shur, *IEEE Sensors Journal* **21** (11), 12752 (2020).
- ⁵ Craig Kulesa, *IEEE Transactions on Terahertz Science and Technology* **1** (1), 232 (2011).
- ⁶ T.R. GLOBUS, D.L. WOOLARD, T. KHROMOVA et al., *Journal of Biological Physics* **29**, 89 (2003).
- ⁷ Cecilie Rønne, Per-Olof Åstrand, and Søren R. Keiding, *Physical review letters* **82** (14), 2888 (1999).
- ⁸ M Tonouchi, *Nature Photonics* **1** (2), 97 (2007).
- ⁹ M. Shur, S. Rudin, G. Rupper et al., *Solid-State Electronics* **155**, 44 (2019).
- ¹⁰ Thomas George, Achyut K. Dutta, M. Saif Islam et al., presented at the Proceedings of SPIE, 2018 (unpublished).
- ¹¹ Stéphane Blin, Frédéric Teppe, Lucie Tohme et al., *IEEE Electron Device Letters* **33** (10), 1354 (2012).
- ¹² Tadao Nagatsuma, *IEEE Photonics Journal* **6** (2), 1 (2014).
- ¹³ Sergey Romyantsev, Guanxiong Liu, Radislav A. Potyrailo et al., *IEEE Sensors Journal* **13** (8), 2818 (2013).
- ¹⁴ C. W. Berry, N. Wang, M. R. Hashemi et al., *Nat Commun* **4**, 1622 (2013).
- ¹⁵ T. W. Crowe, R. J. Mattauch, H. P. Roser et al., *Proceedings of the IEEE* **80** (11), 1827 (1992).
- ¹⁶ Michael I. Dyakonov and Michael S. Shur, *IEEE Transactions on Electron Devices* **43** (10), 1640 (1996).
- ¹⁷ Michel I. Dyakonov, *Comptes Rendus Physique* **11** (7-8), 413 (2010).
- ¹⁸ V. Ryzhii, T. Otsuji, and M. Shur, *Applied Physics Letters* **116** (14) (2020).
- ¹⁹ D. A. Bandurin, D. Svintsov, I. Gayduchenko et al., *Nature Communication* **9** (1), 5392 (2018).
- ²⁰ Yuhui Zhang and Michael S. Shur, *IEEE Transactions on Electron Devices* **67** (11), 4858 (2020).
- ²¹ Michael Shur, Sergey Rudin, Greg Rupper et al., *Applied Physics Letters* **113** (25), 253502 (2018).
- ²² Yuhui Zhang and Michael S. Shur, *Journal of Applied Physics* **129** (5), 053102 (2021).
- ²³ M. V. Cheremisin, M. I. Dyakonov, M. S. Shur et al., *Solid-State Electronics* **42** (9), 1737 (1998).
- ²⁴ M. Dyakonov and M. Shur, *IEEE Transactions on Electron Devices* **43** (3), 380 (1996).

- ²⁵ M. Shur, S. Rudin, G. Rupper et al., *IEEE Photonics Newsletter* **33** (3), 4 (2019).
- ²⁶ Gregory J. Exarhos, Lars O. Jensen, Vitaly E. Gruzdev et al., in *Laser-Induced Damage in Optical Materials: 2010* (International Society for Optics and Photonics, 2010), Vol. 7842, p. 784207.
- ²⁷ M. B. Zahid, R. Degraeve, L. Pantisano et al., in *2007 IEEE International Reliability Physics Symposium Proceedings. 45th Annual* (2007), pp. 55.
- ²⁸ J. Buckley, B. De Salvo, G. Ghibauda et al., *Solid-State Electronics* **49** (11), 1833 (2005).
- ²⁹ S. Norasetthekul, P.Y. Park, K.H. Baik et al., *Applied Surface Science* **187** (1-2), 75 (2002).
- ³⁰ S. Rudin, G. Rupper, A. Gutin et al., *Journal of Applied Physics* **115** (6), 064503 (2014).
- ³¹ Michael Shur, *Introduction to electronic devices*. (J. Wiley, 1996).
- ³² Y.H. Byun, K. Lee, and M. Shur, *IEEE Electron Device Letters* **11** (1), 50 (1990).
- ³³ Michael Shur, *Applied Physics Letters* **54** (2), 162 (1989).
- ³⁴ Michel I Dyakonov and Michael S Shur, in *Future Trends in Microelectronics: Up the Nano Creek* (John Wiley & Sons, 2007), pp. 296.
- ³⁵ V. Yu Kachorovskii and M. S. Shur, *Applied Physics Letters* **100** (23) (2012).
- ³⁶ Tomohisa Mizuno, Jun-ichi Okamura, and Akira Toriumi, *Applied Physics Letters* **41** (11), 2216 (1994).
- ³⁷ Hoik Lee, Keewook Paeng, and Ick Soo Kim, *Synthetic Metals* **244**, 36 (2018).
- ³⁸ M. Dyakonov and M. Shur, *Physical review letters* **71** (15), 2465 (1993).
- ³⁹ Pedro Cosme and Hugo Terças, *Applied Physics Letters* **118** (13) (2021).
- ⁴⁰ M. V. Cheremisin and G. G. Samsonidze, *Semiconductors* **33** (5), 619 (1999).
- ⁴¹ Christian B. Mendl and Andrew Lucas, *Applied Physics Letters* **112** (12) (2018).
- ⁴² Christian B. Mendl, Marco Polini, and Andrew Lucas, *Applied Physics Letters* **118** (1) (2021).
- ⁴³ Yuhui Zhang and Michael S. Shur, *IEEE Transactions on Electron Devices* **68** (2), 903 (2020).
- ⁴⁴ A. P. Dmitriev, A. S. Furman, and V. Yu. Kachorovskii, *Physical Review B* **54** (19), 14 020 (1996).
- ⁴⁵ Pedro Cosme and Hugo Terças, *ACS Photonics* **7** (6), 1375 (2020).
- ⁴⁶ Greg Rupper, Sergey Rudin, and Frank J. Crowne, *Solid-State Electronics* **78**, 102 (2012).
- ⁴⁷ W. Knap, V. Kachorovskii, Y. Deng et al., *Journal of Applied Physics* **91** (11), 9346 (2002).
- ⁴⁸ A. Gutin, V. Kachorovskii, A. Muraviev et al., *Journal of Applied Physics* **112** (1), 014508 (2012).
- ⁴⁹ Zeen Huang, Yuhui Zhang, Dong Dai et al., *AIP Advances* **11** (1) (2021).
- ⁵⁰ Frank Stern, *Physical review letters* **44** (22), 1469 (1980).
- ⁵¹ Tsuneya Ando, Alan B. Fowler, and Frank Stern, *Reviews of Modern Physics* **54** (2), 437 (1982).
- ⁵² S. Takagi, A. Toriumi, M. Iwase et al., *IEEE Transactions on Electron Devices* **41** (12), 2357 (1994).
- ⁵³ I. V. Gorbenko, V. Y. Kachorovskii, and M. Shur, *Opt Express* **27** (4), 4004 (2019).
- ⁵⁴ W. Knap, E. Borovitskaya, M. S. Shur et al., *Applied Physics Letters* **80** (7), 1228 (2002).
- ⁵⁵ R. Gaska, M. S. Shur, A. D. Bykhovski et al., *Applied Physics Letters* **74** (2), 287 (1999).
- ⁵⁶ Ikuko Akimoto, Yushi Handa, Katsuyuki Fukai et al., *Applied Physics Letters* **105** (3), 032102 (2014).
- ⁵⁷ Nobuko Naka, Katsuyuki Fukai, Yushi Handa et al., *Physical Review B* **88** (3), 035205 (2013).
- ⁵⁸ G. R. Aizin, J. Mikalopas, and M. Shur, *Physical Review B* **101** (24), 245404 (2020).